Nano Research

Open Access

Research Article

High oxygen transport electrode with long-term stability for high-power and low Pt-loaded proton exchange membrane fuel cells

Huiyuan Li[1], Jiabin You[1], Shu Yuan[1], Enping Wang[1], Xiaojing Cheng[1], Liuxuan Luo[1], Xiaohui Yan[1], Shuiyun Shen[1,2] ✉, and Junliang Zhang[1,2]

[1] *Institute of Fuel Cells, School of Mechanical Engineering, Shanghai Jiao Tong University, Shanghai 200240, China*
[2] *MOE Key Laboratory of Power & Machinery Engineering, Shanghai Jiao Tong University, Shanghai 200240, China*

Cite this article: *Nano Research*, **2026**, *19*, 94908445. https://doi.org/10.26599/NR.2026.94908445

ABSTRACT: The reduction of Pt loading in cathode catalyst layers (CCLs) of proton exchange membrane fuel cells (PEMFCs) leads to increased local oxygen transport resistance (R_{local}) through the ionomer-Pt interface on triple phase boundaries (TPBs), as well as poor durability due to key material degradation. This work introduces a stable and accessible porous carbon featuring a graphitized structure as well as optimized pore size of carbon supports, thereby achieving a comprehensive ionomer/catalyst interface. The results show that the graphitization degree of the carbon surface increased significantly after modification, and the slight thermal corrosion facilitates the conversion of micropores into accessible pores between 4–7 nm on carbon surface. The polarization curves exhibit that the peak power density of catalyst based on modified EC300J is 38% higher than the catalyst with conventional carbon supports EC300J (Pt/porous carbon catalyst) under standard operating conditions, and R_{local} decreased from 0.35 to 0.08 s·cm^{-1}. It is demonstrated that the positively charged carbon surface and optimized pore size on the Fe graphitized carbon supports provide facile and efficient oxygen transport on TPBs. The higher degree of graphitization also provides improved durability, with less performance loss (8.8%) after degradation compared to the baseline electrode (55.2%).

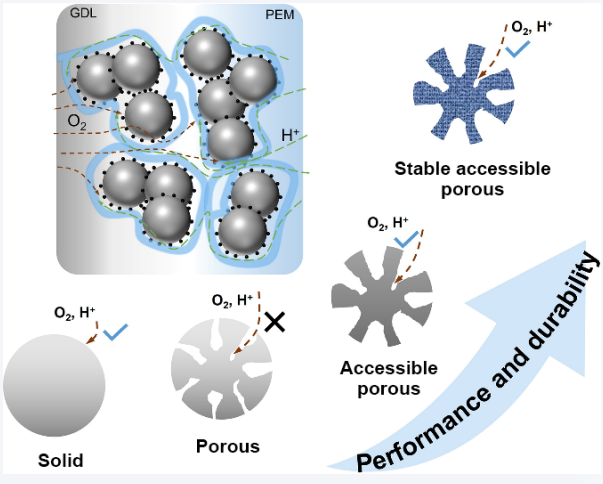

KEYWORDS: proton exchange membrane fuel cells (PEMFCs), carbon support, local oxygen transport, triple phase boundary, durability

1 Introduction

The growing concern over carbon dioxide (CO_2) emissions resulting from the use of fossil fuels and their contribution to climate change has led to an increasing global shift towards renewable energy sources [1]. However, the major barrier lies in a fundamental disparity between renewable and conventional energy sources, as renewable energy exhibits inherent instability and unpredictability, with its output being highly contingent upon weather conditions and time [2]. Hydrogen has recently emerged as a promising storage medium and acts as a clean and efficient solution for a sustainable energy system. Proton exchange membrane fuel cells (PEMFCs) can electrochemically convert chemical energy to electricity and are widely regarded as next-generation power devices because of their high efficiency and zero emissions [3, 4].

Nevertheless, the high cost of platinum (Pt)-based electrocatalyst in cathode catalyst layers (CCLs) of PEMFCs remains to be tackled for their wide commercialization [5]. The Pt loading used in membrane electrode assemblies (MEAs) should be reduced to 0.125 mg_{Pt}·kW^{-1} to reach the United States Department of Energy (US DOE) ultimate target of \$30 kW^{-1} [6]. The oxygen reaction reduction (ORR) rate and active site utilization in CCLs are significantly influenced by the transport of oxygen and protons due to their complex porous structure, as illustrated in Fig. 1(a). Continuous reduction of noble Pt-based catalysts restricts the high performance due to the high oxygen transport resistance in CCLs,

Received: October 23, 2025; **Revised:** December 17, 2025
Accepted: January 10, 2026

✉Address correspondence to shuiyun_shen@sjtu.edu.cn

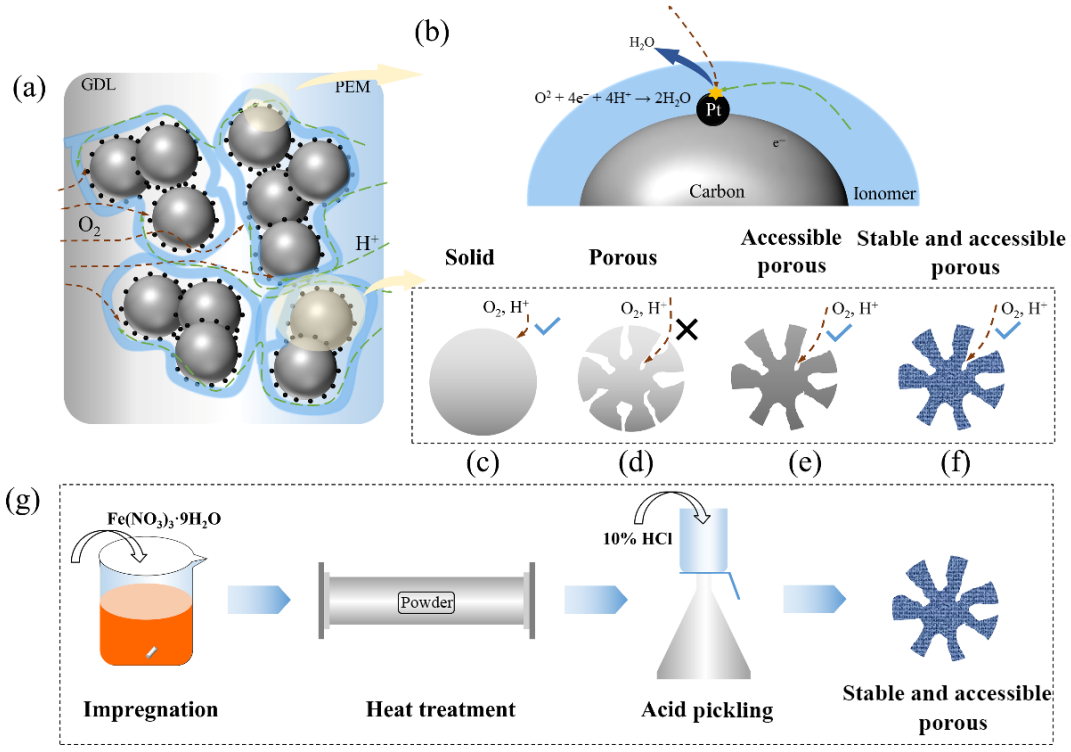

Figure 1 Oxygen transport mechanism and carbon support types. (a) Oxygen and proton transport in CCLs; (b) morphology and oxygen transport mechanism of triple phase boundary; ((c)–(f)) oxygen transport mechanism for solid, porous, accessible porous, and stable accessible porous carbon; and (g) schematic of catalytic graphitization process via metal nanoparticles.

especially the local oxygen transport resistance (R_{local}) on the triple phase boundaries (TPB) consisting of carbon-supported catalyst for ORR and electronic conduction, perfluorinated sulfonic acid (PFSA) ionomer for proton conduction, and reactant gas phase, as shown in Fig. 1(b) [7, 8]. In addition, the stability of TPBs is also announced as the catalyst loading declines, which should be considered as the US DOE ultimate target of fuel cell vehicles has been prolonged for 8000 cycles [6].

In recent years, researchers have stressed the vital role of carbon supports for highly efficient TPBs in enabling high catalyst activity and high oxygen transport at low Pt loadings [9–11]. The carbon supports processes enlarged surface area, which improves the deposition of catalyst nanoparticles, and the ORR activity by decreasing the Fermi level, making the performance improve 10-fold compared to the Pt black catalyst [12, 13]. Carbon supports play a crucial role in shaping the intricate pore structure in CLs with the ionomer thin film coating on its surface, as well as catalyst nanoparticles, which serve as a conduit for proton conduction while impeding oxygen transport. However, the thermodynamic instability of carbon material renders it susceptible to oxidation, which could lead to a severe performance loss due to complex degradation of the incorporation of ORR activities and mass transport on TPBs [14]. Thus, a comprehensive catalyst/carbon/ionomer TPB should be established, which is closely related to carbon surface morphology and consists of (i) physicochemical properties and (ii) pore structure.

The physicochemical properties on the carbon surface, such as wettability and surface charge effect, not only make sense on the deposition of catalyst nanoparticles, but also influence the ionomer distribution, and in turn alleviate the oxygen transport issue at the TPBs [15]. As shown in Fig. 1(b), the ionomer film covering on the catalyst surface is expected to be uniformly distributed, rather than forming the inhomogeneous ionomer aggregations, in order to facilitate the proton conduction and oxygen transport. Effective regulation strategies on carbon surface should be proposed to optimize the TPB structure and enhance oxygen transport in CCLs. This is mainly determined by the interaction between carbon surface and the PFSA ionomer with sidechain (sulfonic groups, $-SO_3H$) and backbone (polytetrafluoroethylene (PTFE)). The effects of the carbon surface oxygen ratio on the interaction between the carbon surface and ionomer were investigated by Zhao et al [11]. They found that the moderate oxygen ratio (2.5% oxygen) could lead to the strong combination of both the hydrophilic and hydrophobic interface near or next to the catalysts, which results in a uniform distribution of the ionomer. Ott et al. [16, 17] functionalized carbon surface with balanced quantities of stable pyridinic and pyrrolic N groups. The strong acidity of the ionomer leads to protonation of the N-groups through an acid-base interaction between the sulfonic sidechain and the basic N-species, thereby facilitating a homogeneous spatial distribution of ionomer film in CCLs. Li et al. [18] engineered an ideal ionomer/catalyst interface by grafting a positively charged pbenzylamine group ($-NH_3^+$ after hydration) covalently on the carbon surface in a catalyst ink and preserved in a solid CL. These functional groups on the carbon surface show a strong interaction with the negatively charged sulfonic groups in the ionomer particles and form a much more uniform and thinner ionomer film. Moreover, the flooding in CCLs, which negatively affects both the bulk and local oxygen transport, can be mitigated by optimizing TPBs by adjusting the hydrophobicity of the carbon surface while ensuring satisfactory proton conductivity [11, 19].

The pore structure on carbon surface also plays a crucial role in determining both oxygen transport and stability of TPBs. Current carbon supports can be broadly classified into solid (Fig. 1(c)) and

porous (Fig. 1(d)) types, where the surface area for the solid one (e.g., ~ 230 $m^2 \cdot g_C^{-1}$ for Vulcan carbon) is far lower than the porous one (e.g., ~ 800 $m^2 \cdot g_C^{-1}$ for Ketjenblack EC300J). The large surface area is advantageous for the catalyst deposition and widely accepted for Pt particle deposition within micropores to mitigate the ORR activity poisoning on Pt catalyst by sulfonic groups [20]. However, interior pores on the carbon surface can be tortuous, and the catalyst particles protected within have restricted access to protons and oxygen. The transport mechanism of oxygen in porous carbon undergoes changes from the solid carbon because of the difference in the interaction between carbon surface and ionomer for the two kinds of carbon supports. Specifically, ionomer is located on the surface of the catalyst deposited on the solid carbon, and R_{local} refers to the oxygen transport resistance through the ionomer. On the other side, the ionomer is located outside the nano-sized pores on the porous carbon surface [20]. Thus, the proton is conducted based on ionomer in the exterior surface and water within the interior pores, while the R_{local} consists of oxygen transport resistance in ionomer ($R_{ionomer}$) in the exterior surface and in pores (R_{pore}). Ramaswamy et al. [21] and Yarlagadda et al. [20] observed that R_{local} increases as the volume of nanopores (< 2 nm) increases due to potential bottleneck effects caused by micropore openings in the carbon supports. Conversely, it decreases as the volume of the mesopores (4–7 nm) increases, resulting in shorter transport lengths on TPBs for better proton and oxygen accessibility, which is called accessible porous carbon in Fig. 1(e). Therefore, the pore size design is indispensable for the balance of ORR activity and the oxygen transport process. The desirable mesopores with a preferred pore opening should be designed to give catalysts with both excellent ORR activities and oxygen transport properties, especially in low Pt loading MEAs.

In addition, the carbon oxidation tolerance of porous carbon is inferior to that of solid carbon due to larger amorphousness and less graphitization [22], which makes the faster failure towards start-up/shut-down (SUSD) degradation. Thus, the maintenance of stability in the accessible porous carbon and the acquisition of stable accessible porous carbon, as depicted in Fig. 1(f), are crucial. The graphitized carbon (GC) is widely considered as a feasible solution for the stable cathode catalyst support material [23]. The traditional and well-applied method for carbon graphitization is high-temperature heat treatment at a temperature above 2000 °C to provide energy for atomic rearrangement and structural transformation. It allows the use of thermal activation to achieve the orderly transformation of thermodynamically unstable carbon atoms from chaotic layer structure to graphite crystal structure [24, 25]. However, the acquisition of porous carbon through this method is challenging due to the carbon precursor surface structure damage incurred by the traditional process. Additionally, the high experimental operating temperatures and lack of environmental friendliness further hinder the implementation of this traditional process.

In this case, the graphitization process must be optimized to cater to the demands of porous carbon in PEMFCs, so as to enhance the advantages of ORR activity and durability. Researchers have reported a catalytic graphitization method with the aid of metal particles (e.g., Fe, Co, Mn, and Ni) to enhance the crystallization of carbon by a chemical reaction between the catalyst (metal or an inorganic compound) and amorphous carbon [26, 27]. This catalytic graphitization method requires only relatively low temperatures (< 1000 °C), which results in slight destruction of the surface structure. It is noted that the metal nanoparticles are not only capable of catalyzing graphitization but also adept at regulating pore structure, thus facilitating the attainment of the aforementioned "accessible porous carbon" morphology.

Here, we proposed a novel catalyst through utilizing the catalytic graphitization method as illustrated in Fig. 1(g). The enhanced graphitization degree and optimized pore size distribution led to the development of a stable and accessible porous carbon support and efficient ionomer/catalyst interface. Subsequently, the surface microstructure and property changes of the metal graphitized carbon supports were assessed by physicochemical characterizations. The performance and durability of the MEA based on the catalyst with Fe graphitized carbon supports were measured systematically in conventional single-layer electrodes.

2 Experiment

2.1 Carbon graphitization and catalyst synthesis

Commercial porous carbon supports Ketjenblack EC300J (Cabot) were received as the porous carbon precursor. A large number of nanopores in the EC300J enabled uniform adsorption of the ions, which played an important role in the growth of controllable graphitic nanostructures during subsequent catalytic graphitization. Specifically, the EC300J precursor was impregnated in $Fe(NO_3)_3 \cdot 9H_2O$ (Aladdin) solutions overnight. After vacuum drying, the mixture was put in a quartz tube furnace for sintering under nitrogen flow. The samples were subjected to graphitization at a temperature of 900 °C for a duration of 6 h, employing a heating rate of 5 °C·min^{-1}. Subsequently, they were cooled down to room temperature. Finally, the products were washed with 1 M HCl (Aladdin) 3 times at 80 °C to remove the nickel residue.

Then the Pt-based catalyst was synthesized by depositing Pt on the initial or modified EC300J carbon via polyol-method. 300 mg of the carbon support was mixed with 200 mL of ethylene glycol (Aladdin), 100 mL of ultrapure water (Millipore, > 18.2 MΩ·cm), and 1.35 mL of 0.25 mol·L^{-1} H_2PtCl_6 (Sinopharm Chemical Reagent Co., Ltd.) solution. The dispersion was stirred for 18 h at 25 °C and then for 2 h under reflux conditions at 120 °C. The slurry was then filtered, washed with hot ultrapure water, and finally dried in an air oven at 70 °C overnight. Then, the prepared catalysts were annealed at 250 °C for 1 h in a reducing environment (95% Ar and 5% H_2).

2.2 Rotating disk electrode (RDE) measurement

RDE tests were carried out with a CHI660D potentiostat (CH Instruments) at room temperature in three-electrode cells. A glassy carbon rotating disk (area: 0.196 cm^2) coated with the corresponding catalyst was used as the working electrode. A saturated calomel electrode and a 1 cm^2 Pt foil were used as the reference and counter electrodes, respectively. The potentials in this study are all referenced to the reversible hydrogen electrode (RHE). The Pt/porous carbon, and Pt/Fe graphitized porous carbon catalysts were dispersed in a mixed solvent containing ultrapure water, ethanol, and ionomer (Nafion, DuPont, 20 wt.%) as the catalyst binder to obtain homogeneous catalyst ink. After a 30 min sonification, a droplet of 7 μL of each ink was placed on the rotating disks representing the respective working electrodes.

The ORR electrocatalytic activity (i.e., the ORR kinetic current density) is evaluated by the forward linear sweep voltammogram (LSV) obtained at 10 mV·s^{-1} with a rotating rate of 1600 rpm in an

O_2-saturated 0.1 M $HClO_4$ (Aladdin) solution. The cyclic voltammetry (CV) technique was used to determine the electrochemically active surface area (ECSA) via integrating the hydrogen desorption charge from CV at a rate of 20 mV·s^{-1} in N_2-saturated 0.1 M $HClO_4$ solution. The current was normalized to the Pt amount to get the mass activity.

2.3 MEA preparation and single-cell measurement

All MEAs were electrostatic sprayed on each side of PEMs (DuPont, Nafion 211, and Gore M765.08) to form MEAs. The anode catalyst layer (ACL) and CCL ink catalysts were prepared by mixing the Pt/C catalysts, ionomer solution (Nafion, DuPont, 20 wt.%), as well as ethanol and ultrapure water employed as solvents. The ionomer to carbon weight ratio (I/C) was 0.6. A dual-layer CCL design was involved for oxygen transport resistance quantification [28]. It consisted of a real CCL and a dummy catalyst layer (DCL) with varying thicknesses, wherein the corresponding carbon supports for the catalysts were substituted in place of the actual catalyst in the CCL ink and incorporated into the DCL ink. The cathode catalyst loading was 0.08 $mg_{Pt}·cm^{-2}$ for polarization curves, Tafel plots, ECSA, and electrochemical impedance spectroscopy (EIS) measurements, and 0.05 $mg_{Pt}·cm^{-2}$ for the dual-layer CCL design, utilizing TEC10E30E, Pt/porous carbon, and Pt/Fe graphitized porous carbon catalysts, respectively. The anode catalyst loading, using TEC10E30E, was 0.05 $mg_{Pt}·cm^{-2}$ for all MEAs.

Single cells were fabricated with the as-made MEAs and gas diffusion layers (GDLs, Ballard, GDS3250) for the next electrochemical measurements. The fuel cell performance of the conventional single-layer electrode with an active area of 25 cm^2 and a single serpentine flow field was characterized by polarization curves using H_2 and air at the anode and cathode. The stoichiometric ratio, relative humidity (RH), operating pressure, and temperature were set as 2/2, 100%, 150 kPa_{abs} (where abs denotes absolute pressure), and 80 °C, respectively. The mass specific activity of the cathode catalyst was characterized by Tafel curves in an H_2/O_2 cell at 100% RH, 150 kPa_{abs}, and 80 °C. The ECSA of the cathode catalyst was characterized using CV in an H_2/N_2 cell at 100% RH, 100 kPa_{abs}, and 80 °C, and the sweep rate was 20 mV·s^{-1}.

Limiting current densities [29] were measured using fuel cells with an active area of 2 cm^2 with a parallel 10-pass configuration. Pure H_2 and 4 mol% O_2–N_2 gas mixture were used at the anode and cathode, respectively, and the RH, operating pressure, and temperature were 67%, 150 kPa_{abs}, and 80 °C, respectively. The constant flow rate of reactant gas was 0.8 L·min^{-1} for the anode and 1.5 L·min^{-1} for the cathode. The voltage sweep range was 0.8–0.05 V, and the linear sweep rate was 5 mV·s^{-1}.

EIS in H_2/air was implemented in a single cell with an active area of 25 cm^2 to measure overall internal resistance of the PEMFC. The frequency was swept from 20 kHz to 0.5 Hz (0.2/0.2 L·min^{-1}) at 100% RH. EIS in H_2/N_2 was implemented in a single cell with an active area of 25 cm^2 to measure the effective through-plane proton conduction resistance of the cathode electrode ($R_{H^+,cath}$). The frequency was swept from 10 kHz to 0.5 Hz with H_2/N_2 (0.2/0.2 L·min^{-1}) at 100% RH.

The carbon-corrosion effects and degradation behaviors of the three catalysts were characterized via employing an accelerated stress test (AST) protocol from the US DOE [6]. The cathode loading of the MEAs was 0.05 $mg_{Pt}·cm^{-2}$, employing TEC10E30E, Pt/porous carbon, and Pt/Fe graphitized porous carbon catalysts, respectively. The anode loading, using commercial catalyst TEC10E30E, was 0.05 $mg_{Pt}·cm^{-2}$ for the three MEAs. Triangle wave potential cycling between 1.0 and 1.5 V at 500 mV·s^{-1} in an H_2/N_2 configuration at 80 °C and 100% RH was conducted to isolate Pt dissolution and growth and study only carbon corrosion and its subsequent effects. Samples were subjected to 3000 cycles, and then a recovery voltage cycle was conducted to counteract the reversible loss in the steady-state AST [30].

2.4 Characterization method

The size of ionomer aggregation in the catalyst ink and the potential of the carbon supports were observed by a particle size and zeta potential analyzer (Brookhaven Instruments Corporation, Model: Omni). The concentration of Fe in the catalyst was measured by inductively coupled plasma-optical emission spectroscopy (ICP-OES, Thermo iCAP6300). The morphologies of CLs were characterized using transmission electron microscope (TEM, Talos F200X G2 and Thermo Scientific), scanning electron microscope (SEM, JEOL JSM-6700F, and ZEISS Gemini 360), and atomic force microscope (AFM, Dimension XR). Carbon surface chemistry was analyzed based on X-ray photoelectron spectroscopy (XPS, Thermo ESCALAB 250Xi). X-ray diffraction (XRD) analysis was carried out on a Bruker D8 ADVANCE DA VINCI X-ray diffractometer with Cu Kα radiation (λ = 0.154 nm). Raman spectra were recorded in a Renishaw in Via Raman microscope using the 532 nm lasers as a light source. Specific surface area and the pore size distribution were calculated using a quenched solid density functional theory (QSDFT) kernel for slit/cylindrical pores (Autosorb-IQ3), and the porosity of CCLs was measured using mercury porosimeter (MIP, Micromeritics, AutoPore 9510). The apparent contact angles of each initial and modified carbon support were measured by a drop shape analyzer (DSA100S, KRÜSS Scientific).

3 Results and discussion

3.1 Design and construction of the carbon surface

The precursor carbon supports EC300J is extensively utilized for ORR catalysts due to its significantly high surface area and abundant pores, which, however, hinder the oxygen and proton transport especially in micropores. The method of catalytic graphitization via Fe nanoparticles is employed for the morphology and structure design on the carbon surface of EC300J [31], as shown in Fig. 1(g). The as-received powder mixture is then heat-treated under an inert atmosphere (i.e., N_2). During this process, $Fe(NO_3)_3$ decomposes with the formation of the corresponding metallic oxides, which is subsequently reduced by carbon at elevated temperatures and results in a slight thermal corrosion of EC300J carbon based on Eq. (1). Finally, in contrast to the conventional graphitization method that typically necessitates high temperatures (> 2000 °C) to convert surface carbon atoms from a disordered layered structure into a crystalline graphitic structure, the inclusion of metal or oxide nanoparticles within the carbon pores and on its surface acts as catalysts to the transform the amorphous carbon into more ordered (graphitic) forms at significantly lower temperatures (i.e., 700–900 °C) [32]

$$C + Fe_2O_3 \rightarrow CO/CO_2 + Fe \quad (1)$$

The Fe nanoparticles attached to the carbon supports are washed

with 0.1 M HCl solutions at 80 °C after heat treatment. The ICP results show that the Fe content decreased from 34.6 wt.% to 1.4 wt.% after acid washing, corresponding to 96% of the total metal. The remaining Fe is considered to be negligible, thus it will have no impact on the performance of the catalyst.

The carbon supports are firstly impregnated with $Fe(NO_3)_3$ with the addition of 12 $mmol_{Fe} \cdot g_C^{-1}$, undergoing the 900 °C. TEM images of pristine EC300J and modified EC300J carbon supports are employed to identify the degree of graphitization on carbon surface. The disordered and amorphous carbon surface is depicted in Fig. 2(a). The high resolution-TEM (HRTEM) image confirms the absence of ordered graphitic domains with an approximate spacing of 0.4906 nm. The modified EC300J carbon surface exhibits a significant graphitic nature compared to the pristine carbon, as highlighted by the red circles in Fig. 2(b). The carbon sheet spacing is measured to be 0.3485 nm, which is significantly smaller than that of the pristine carbon surface. The morphology on the carbon surface via the conventional high temperature method and the catalytic graphitization method is compared to ensure the degree of graphitization. TEM images of highly graphitized carbon EA (a commercial carbon originated from Shanghai Tangfeng Energy Technology Co., LTD) are shown in Fig. S1 in the Electronic Supplementary Material (ESM). This carbon was graphitized at a temperature above 2000 °C via a conventional graphitization method, and its sheets spacing is measured to be 0.3032 nm. It is demonstrated that the conventional high-temperature treated method provides highly ordered graphitized structure. This observation of a slightly larger EA spacing than that of modified EC300J indicates the existence of turbostratic carbon [31–33]. This unique structure comprises polyaromatic sheets with sufficient defects and exhibits rotational and translational disorder, which enables effective resistance against carbon corrosion without weakening the catalyst deposition on the carbon surface.

Figure 2(c) shows XRD diffractograms for pristine EC300J and modified EC300J carbon supports. The sharper and narrower diffraction peaks at ~ 26° and ~ 43° are attributed to the (002) and (101) graphitic planes, demonstrating an increased degree of graphitization after modification. The level of graphitization was further confirmed by Raman spectroscopy, as depicted in Fig. 2(d). Two distinct peaks are seen at 1340 and 1575 cm^{-1}, corresponding to the D (disordered) and G (graphitic) bands, respectively. The intensity ratio of D and G bands (I_D/I_G) serves as a reliable indicator for assessing the level of amorphousness, with a lower I_D/I_G ratio corresponding to a higher degree of graphitic structure. The I_D/I_G values are calculated as 1.35 and 0.97 for pristine EC300J and modified EC300J carbon supports, respectively. It demonstrates that the modified EC300J exhibits a more ordered graphitic structure, confirming the effectiveness of the Fe graphitization modification. The Raman spectroscopy for EA is also shown in Fig. S2 in the ESM, and the I_D/I_G value is calculated as 0.69. It is observed that the graphitization degree of graphitized EC300J catalyzed by Fe is not as high as that via the traditional method, which corresponds to the slightly larger carbon sheet spacing observed in the HRTEM images. Moreover, the hydrophilic properties of oxygen-containing functional groups make the surface of carbon support more prone to corrosion.

XPS is one of the powerful surface analytical techniques that can provide more useful information on the nature of the functional groups on the carbon surface. The pristine EC300J and the

Table 1 XPS data of element composition, and C 1s and O 1s deconvolution

	Binding energy (eV)	Pristine EC300J	Modified EC300J
Element content			
C	—	98.1%	98.91%
O	—	1.91%	1.09%
C 1s deconvolution			
C–C	284.8	58.6%	64.4%
C–O	285.7	23.6%	16.5%
O–C=O	287.4	7.3%	6.8%
Carbonate	289.5	5.2%	5.7%
π–π*	291.5	5.4%	6.6%
O 1s deconvolution			
C=O, O–C=O	532.3	57.3%	71.5%
C–O, C–O–C	533.7	42.7%	28.5%

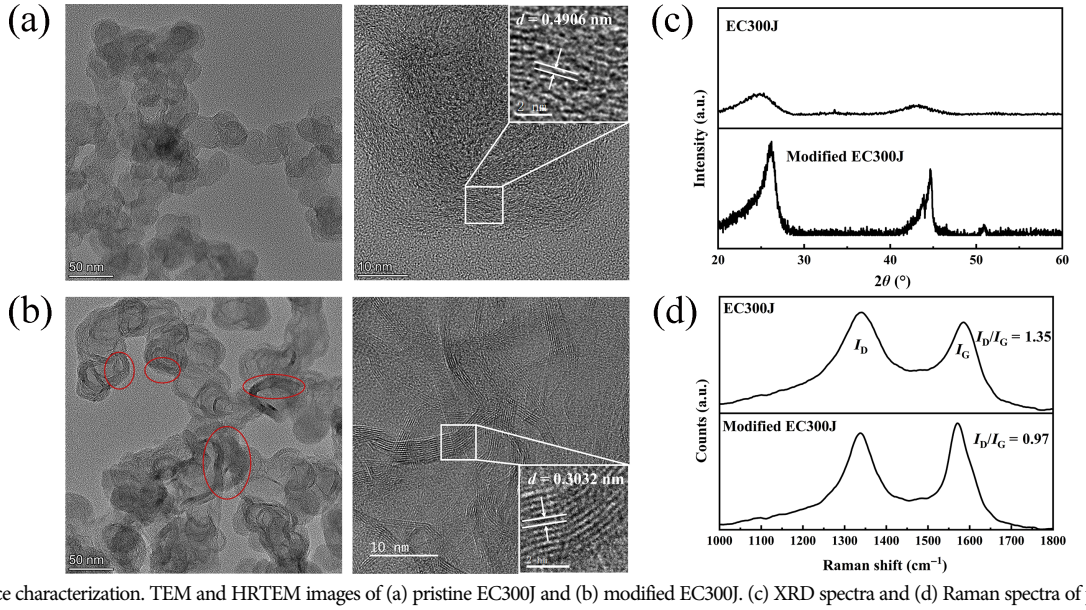

Figure 2 Surface characterization. TEM and HRTEM images of (a) pristine EC300J and (b) modified EC300J. (c) XRD spectra and (d) Raman spectra of pristine EC300J and modified EC300J.

modified EC300J carbon supports are analyzed using XPS, and the results are summarized in Table 1. The survey spectra recorded in the kinetic energy range of 200–1500 eV show a sharp decrease of the oxygen content on the carbon surface from 1.91% to 1.09% after graphitized modification. Further, high-resolution spectra for deconvolution of C 1s and O 1s of pristine EC300J and modified EC300J carbon supports are presented in Figs. 3(a) and 3(b). For the deconvoluted C 1s spectra, the peaks at the binding energies of 284.8, 285.7, 287.4, 289.5, and 291.5 eV are assigned to C–C, C–O, O–C=O, Carbonate, and π–π* transition loss peak, respectively [34]. For the deconvoluted O 1s spectrum, the peaks at the binding energies of 533.7 and 532.3 eV are assigned to single bond C–O, C–O–C and double bond C=O, O–C=O, both of which decreased after modification and could increase the resistance to corrosion and change the interaction between ionomer and carbon surface.

Then, the zeta potential (ξ) was employed to investigate the surface chemistry of pristine EC300J and modified EC300J carbon supports, and the result is shown in Fig. 3(c). The mean values of ξ for pristine EC300J and modified EC300J carbon supports dispersed in water are +27.5 and +58.4 mV. The higher potential ξ for modified EC300J carbon supports is believed to be due to the decreased oxygen-containing functional groups in the process of heat treatment [35]. In addition, the corresponding ionomer (i.e., Nafion) in CCLs and the two kinds of carbon supports were separately dispersed in ethanol, respectively, and a comparison was made between the agglomeration particle size with and without ionomer, as illustrated in Fig. 3(d). The I/C for the carbon and ionomer inks is set to be 0.6. The results show that the mean carbon agglomeration size for the pristine EC300J and modified EC300J is 418 and 270 nm in the inks. It is noted that the statistical results indicate the smaller carbon agglomeration particle size for modified EC300J. This can be attributed to the slight carbon corrosion during the traditional process, which is believed to cause a reduction in both the size of individual carbon particles and carbon agglomerations within the inks. Further, it is observed that the particle sizes for both pristine EC300J and modified EC300J carbon supports are increased after the addition of ionomer due to the attraction of carbon surface and the negatively charged sulfonic groups of the ionomer. However, the extent of particle size increase varies, with pristine EC300J carbon supports experiencing a 13.6% increase in particle size and modified EC300J carbon supports experiencing a more significant increase of 47.8%. The presence of a larger number of oxygen-containing functional groups on the carbon surface of pristine EC300J is believed to result in repulsion between the carbon particles and the negatively charged sulfonic groups. The increased agglomeration particle size in inks due to positively charged surface chemistry will alter ionomer distribution, making it easier to generate a uniform ionomer distribution and form an ideal ionomer/catalyst interface [18].

The traditional graphitization process at a high temperature typically destroys the microporous structure. It is contrary to the desired characteristics of ideal carbon supports for efficient Pt deposition for highly ORR activity and optimal pore structure without compromising oxygen transport. In our study, the effect of the slight thermal corrosion in traditional process on the surface pore structure of carbon supports is characterized by N_2 physisorption. The modified EC300J carbon shows a high specific surface area of 608.8 $m^2 \cdot g_C^{-1}$, although it is lower than the pristine EC300J (832.9 $m^2 \cdot g_C^{-1}$) due to the thermal corrosion. The differential pore size distributions and pore volumes for pristine EC300J and modified EC300J carbon supports depicted in Fig. 4(a) are evaluated using a QSDFT kernel for slit or cylindrical carbon pores [36], which could take the carbon heterogeneity into consideration by a single roughness parameter that represents the characteristic scale of surface corrugation [37, 38]. We distinguish pore size by micropores ($V_{<2nm}$), narrow mesopores (V_{2-4nm}), wide mesopores (V_{4-7nm}), and macropores (V_{7-14nm}) in order to investigate the pore size distribution revolution on carbon surface after modification, as shown in Fig. 4(b). Note that the specific pore volume in the macropores ($V_{>14nm}$) segment, mainly representing the interior particle phenomena between aggregations, was ignored. The results demonstrate that following the modification, there was a reduction in the quantity of micropores, while the number of mesopores with pore sizes ranging from 4 to 7 nm exhibited an increase. This phenomenon is suspected to be attributed to the transformation of micropores into mesopores induced by Fe nanoparticles within the micropore. The specific range of pore size, as determined by Yarlagadda et al., is advantageous for facilitating both oxygen and proton transport [20]. It needs to be recognized that some small and shallow pore structures should disappear during slight carbon corrosion as the specific surface area is reduced. The pore size distribution of EA carbon, as shown in

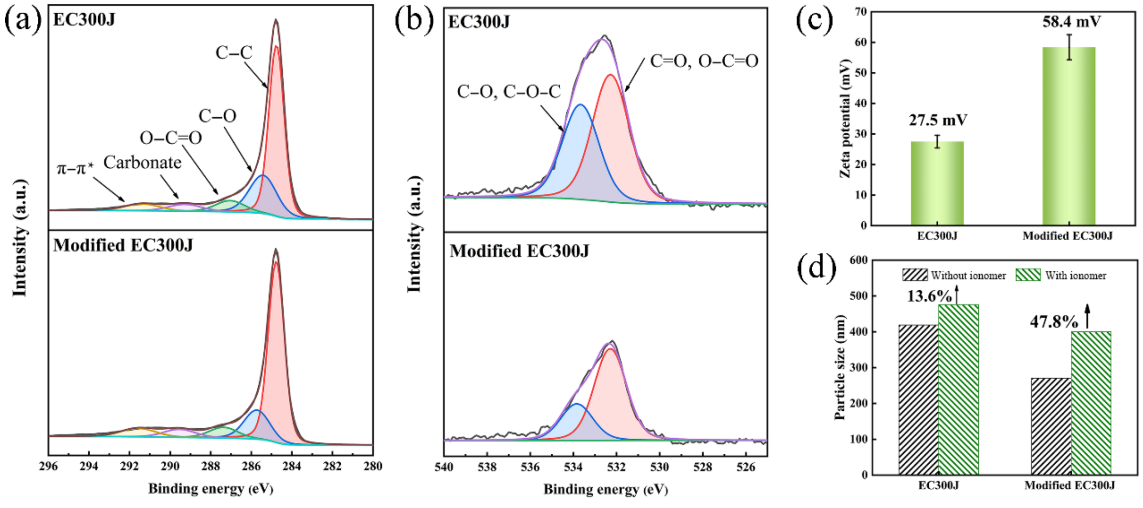

Figure 3 Carbon–ionomer interaction characterization of pristine EC300J and modified EC300J carbon supports. High resolution XPS of (a) C 1s and (b) O 1s spectra. (c) Zeta potential and (d) particle size with and without ionomer.

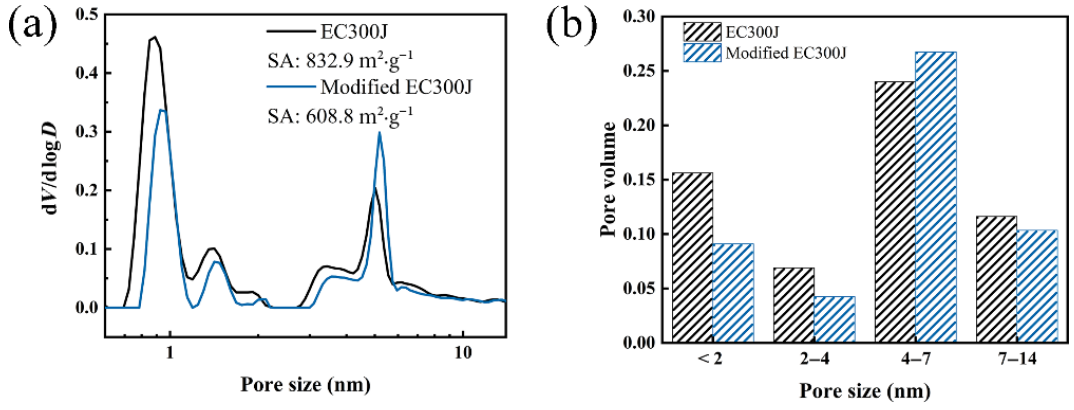

Figure 4 Surface porous structure for the pristine EC300J and modified EC300J carbon supports. (a) Differential pore size distribution determined by N_2 physisorption based on QSDFT. (b) Resulting in specific micro- and meso-pore volumes as segmented in (a).

Fig. S3 in the ESM, reveals a minimal presence of pore structure following the conventional high-temperature graphitization process, with a surface area of 218.8 $m^2 \cdot g_C^{-1}$. This underscores the advantage of the graphitization method catalyzed by Fe, which can increase the graphitization of carbon supports while optimizing the pore structure.

To investigate the influence of different Fe content on the carbon surface graphitized properties and pore size distribution, the carbon supports are then impregnated with $Fe(NO_3)_3$ with additions of 6, 12, and 18 $mmol_{Fe} \cdot g_C^{-1}$, and the XRD and QSDFT methods were conducted. Figure S4 in the ESM shows XRD diffractograms for the three types and original carbon supports. The sharper and narrower diffraction peaks at ~ 26° and ~ 43° attributed to the (002) and (101) graphitic planes demonstrate an increased degree of graphitization with the increased Fe content, which also proves the validity of metal nanoparticles on catalytic graphitization. The differential pore size distributions and pore volumes of pristine EC300J and modified EC300J (with the Fe content of 6, 12, and 18 $mmol_{Fe} \cdot g_C^{-1}$) are depicted in Fig. S5 in the ESM. These data were derived from N_2 physisorption measurements using a QSDFT kernel suited for slit and cylindrical carbon pore models. It is found that when Fe content is 6 $mmol_{Fe} \cdot g_C^{-1}$, the pore within the size of 2–4 nm increases, while when Fe content is 18, the pore structure decreases across all sizes. In addition, the 18 $mmol_{Fe} \cdot g_C^{-1}$ EC300J shows a very low specific surface area of 375.89 $m^2 \cdot g_C^{-1}$, which is not enough to anchor the catalyst nanoparticles. Thus, the optimal addition is 12 $mmol_{Fe} \cdot g_C^{-1}$, as insufficient Fe would impede complete graphitization, while excessive Fe would result in the collapse of the pore structure on the carbon surface. Therefore, in this paper, 12 $mmol_{Fe} \cdot g_C^{-1}$ is selected as the Pt/Fe graphitized porous carbon catalyst for the following electrochemical tests and studies.

3.2 Catalyst electrochemical property

The pristine EC300J and Fe graphitized carbon supports are platinized via a polyol method based on ethylene glycol [39] (Fig. S6 in the ESM), corresponding to Pt/porous carbon, and Pt/Fe graphitized porous carbon catalysts, respectively. The nominal Pt loading of the two catalysts are 16% (±0.3%) determined by ICP, indicating that the modification of the carbon supports does not impact the Pt deposition. The commercial TEC10E30E catalyst is also employed as the control group to illustrate the reasonableness of the polyol process to prepare the homemade catalyst. The morphologies of the three catalysts are determined by TEM images, as shown in Fig. S7 in the ESM, and the insert illustration in each picture is the particle size distribution measured statistically. It is observed that the Pt nanoparticles are uniformly distributed on carbon supports. The particle sizes of Pt in Pt/porous carbon and Pt/Fe graphitized porous carbon catalysts synthesized via the polyol process are 2.78 and 2.95 nm, respectively, which are smaller than the 3.42 nm Pt particles in the commercial TEC10E30E catalyst.

Since TEM uses an electron beam to analyze transmitted electrons, directly visualizing the deposition locations of catalyst nanoparticles (inside vs. outside pores) remains challenging. However, the in-lens detector (InLens) and energy-selective backscattered electron detector (EsB) detectors enable simultaneous dual-channel imaging by capturing secondary electrons (SE) and backscattered electrons (BSE), respectively. The InLens detector (SE mode) resolves fine surface morphological details of the electrode, while the EsB detector (backscattered mode) enhances compositional contrast. This combined approach allows unambiguous identification of Pt nanoparticles at the carbon support interface and within the pores. The SEM images based on the InLens and EsB detectors of the CCL and the catalyst powder are presented in Fig. 5, where the red arrow indicates the catalyst inside the pore, and the yellow arrow indicates the catalyst outside the hole. Roughly 30%–35% of the Pt catalyst nanoparticles are positioned inside the carbon pores (Pt/porous carbon: 31%; Pt/Fe graphitized porous carbon: 35%). The marginally higher percentage found in the modified EC300J can be ascribed to its expanded pore size.

3.3 Electrochemical characterization

ORR activity measurements were performed on the thin film RDE to evaluate the intrinsic catalytic performance of the catalysts. The ORR activities of the Pt/porous carbon, and Pt/Fe graphitized porous carbon catalysts are evaluated by LSV curves as shown in Figs. S8(a) and S8(b) in the ESM, where the mass activities of Pt/porous carbon, and Pt/Fe graphitized porous carbon catalysts are 202.1 and 239.2 $mA \cdot mg_{Pt}^{-1}$ at 0.9 V, respectively. The CV plots are shown in Fig. S8(c) in the ESM, and the ECSA calculated based on the adsorption of hydrogenated species is summarized as 93.1 and 90.1 $m_{Pt}^2 \cdot g_{Pt}^{-1}$ for Pt/porous carbon and Pt/Fe graphitized porous carbon catalysts, respectively. The similar intrinsic mass activities of the catalysts confirm no obvious influence of carbon support graphitization modification on ORR activity. Thus, the discrepancies in performance found during MEA characterizations can be attributed to the difference in CLs structure resulting from support–ionomer interaction and pore structural modifications.

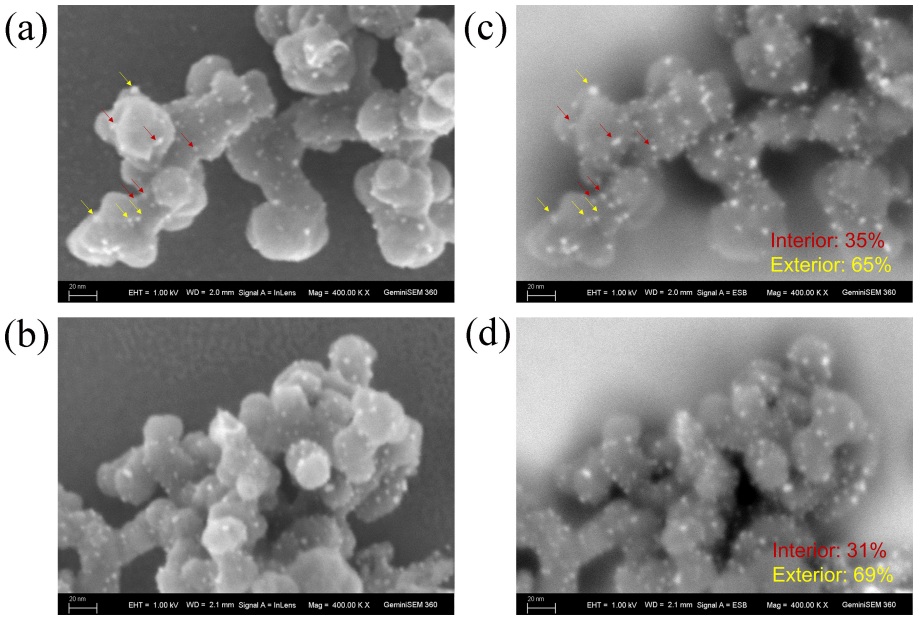

Figure 5 SEM images for the distribution of catalysts. ((a) and (c)) InLens and ((b) and (d)) EsB detectors for ((a) and (b)) Pt/porous carbon and ((c) and (d)) Pt/Fe graphitized porous carbon.

The oxygen and proton transport processes are predominantly controlled by the structure of reaction TPBs, especially in the low Pt loading electrodes. MEAs were conducted with the Pt/porous carbon, and Pt/Fe graphitized porous carbon catalysts as the CLs in order to quantify the impact of the graphitized modification of carbon supports on the MEA performance, which has more complex mass transport and TPBs on account of the interaction among carbon supports, Pt nanoparticles, ionomer and gas phase than the RDE measurements [40].

Specifically, the single-cell fuel cell experiments were conducted on a 25 cm^2 MEA, and the CLs had almost identical Pt loadings of 0.08 $mg_{Pt}·cm^{-2}$ for the cathode electrodes. The TEC10E30E was used as anode catalysts with the Pt loading as 0.08 $mg_{Pt}·cm^{-2}$, and I/C weight ratios for both the cathode and anode are 0.6. The ORR kinetics performance in MEAs was evaluated in a 25 cm^2 single cell with H_2 and O_2 in the anode and cathode at 100% RH, 150 kPa_{abs}, and 80 °C.

The polarization curves of the Pt/porous carbon and Pt/Fe graphitized porous carbon catalysts are investigated as depicted in Fig. 6(a), and the reaction gas, stoichiometric ratio, RH, operating pressure, and temperature are H_2/air, 2/2, 100%, 150 kPa_{abs}, and 80 °C, respectively. The peak power density is 591.4 and 815.7 $mW·cm^{-2}$ for the Pt/porous carbon and Pt/Fe graphitized porous carbon catalysts, respectively. Polarization curve of the Pt/Fe graphitized porous catalysts in high current densities is improved obviously compared to the catalysts based on pristine EC300J catalysts, albeit at low current densities allowing the lower intrinsic ORR kinetics in MEAs. The Tafel plots of the Pt/porous carbon and Pt/Fe graphitized porous carbon catalysts are shown in Fig. 6(b). The mass activities at 0.9 V are 108.4 and 103.2 $mA·mg_{Pt}^{-1}$ for the Pt/porous carbon and Pt/Fe graphitized porous carbon catalysts, respectively, as illustrated in Fig. 6(d). The slight decrease in ORR activity mainly arises from support–ionomer interaction and pore structural modifications. As shown in Fig. 6(c), the EIS spectra are conducted, which exhibit two distinct semicircles with the high-frequency arc corresponding to charge transfer resistance and the low-frequency arc reflecting mass transport resistance. Notably, both the two semicircles for the Pt/Fe graphitized porous carbon are significantly lower than those of Pt/porous carbon at 0.4 V. This confirms that graphitization enhances both charge transfer kinetics and mass transport properties. Therefore, systematic increases in pore accessibility and adjusting surface chemistry should have the most profound effect on the TPBs and accelerate the oxygen transport process.

3.4 Oxygen and proton transport analysis at the TPBs

The altered micropore morphology at the carbon supports interface critically affects cell performance by impeding oxygen and proton transport, as the catalyst's intrinsic activity remains stable. Generally, the concentration polarization in high current densities is dominated by oxygen transport and proton conduction. $R_{H^+,cath}$ are determined from EIS in H_2/N_2 and can be obtained from the magnitude of a Warburg-like region projected onto the real impedance (Z') axis (= $R_{H^+,cath}/3$) [41, 42] as shown in Fig. S9 in the ESM. The $R_{H^+,cath}$ is 111 and 120 $m\Omega·cm^2$ for the MEAs based on Pt/porous carbon and Pt/Fe graphitized porous carbon catalysts.

Ramaswamy has concluded that the change of the macropores is the dominant factor in proton conduction, where the connection of the ionomer covering the pores could be destroyed and restrict the proton conduction with the increased macropores [43]. The little alteration of $R_{H^+,cath}$ after carbon modification, could contribute to the slight change of the macropores ($V_{7–14nm}$) on the carbon surface as discussed in QSDFT measurements. The astonishing performance exhibited by the Pt/Fe graphitized porous carbon catalyst at high current densities can be primarily attributed to the resistance encountered during oxygen transport. Actually, it has been emphasized by many researchers that the R_{local} plays a dominant role in low-Pt-loaded CCLs [7, 44], which is believed to be aided by the pore structure and chemical surface properties of TPBs.

The scanning TEM (STEM) images and corresponding energy-dispersive X-ray spectroscopy (EDX) mapping in Figs. 7(a) and 7(b) reveal the distribution of ionomer on the carbon surface. The cross-sectional cathode samples (80–120 nm thickness, prepared by

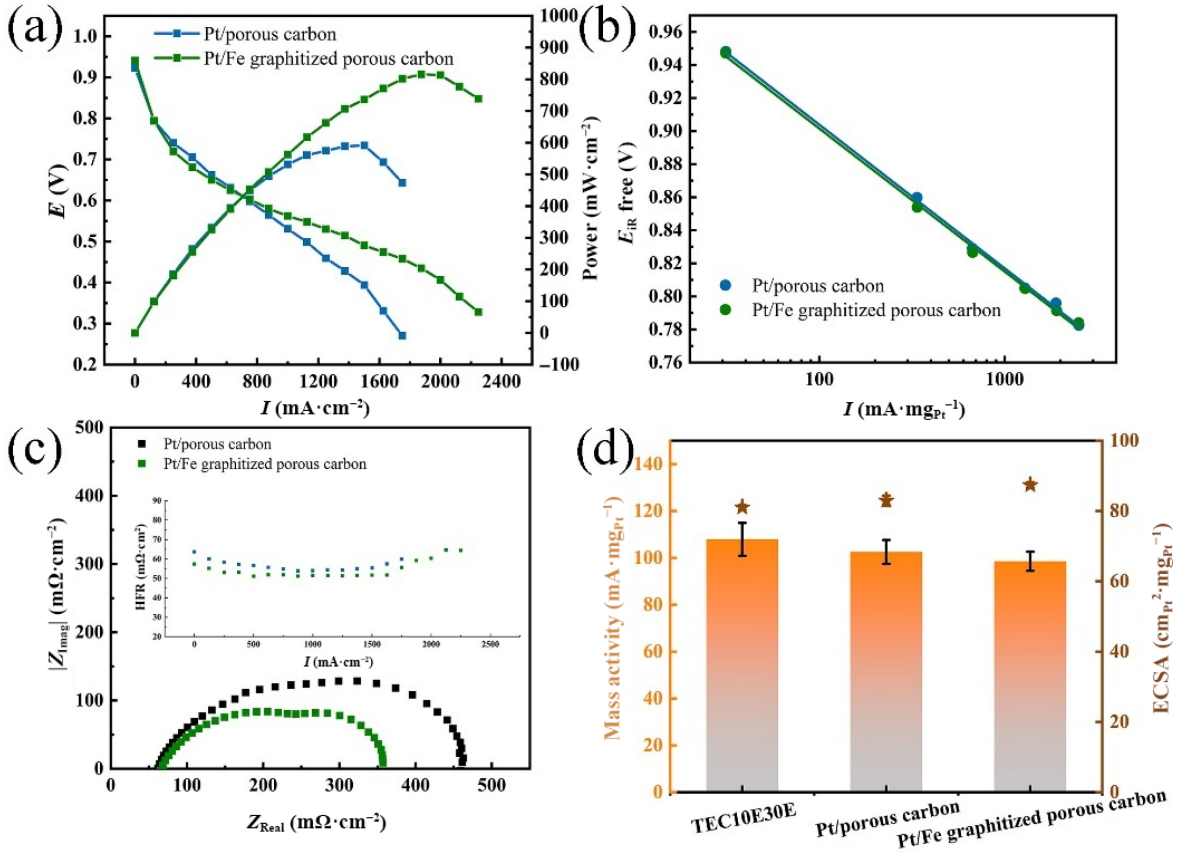

Figure 6 Fuel cell performance in MEA for the Pt/porous carbon and Pt/Fe graphitized porous carbon catalysts. (a) Polarization curves, (b) ORR catalytic activities (Tafel plots), and (c) typical EIS with MEAs based on Pt/porous carbon and Pt/Fe graphitized porous carbon at 0.4 V and high-frequency resistance (HFR) at different current densities (insert). (d) Mass activity extracted from Tafel plots at 0.9 V and ECSA evaluation calculated from the hydrogen under potential deposition region (H_{upd}).

ultramicrotomy) were examined. At the current low ionomer-to-carbon ratio (I/C = 0.6, compared to typical I/C = 0.8–1 in reference [45, 46]), the F signal intensity was inherently weaker due to reduced ionomer content. Nevertheless, Pt/Fe-graphitized carbon CLs exhibited discernible ionomer film contours (average thickness: 2.5 nm), indicating localized aggregation as shown in Fig. S10 in the ESM. Pt/porous carbon CLs showed no distinct ionomer layer boundaries. Thus, the ionomer (dashed box) exhibits enhanced uniformity following carbon modification. Surface modulus mapping (Figs. 7(c) and 7(d)) for the morphology development of CCLs also revealed reduced aggregation size and enhanced uniformity in Pt/Fe graphitized carbon CLs. The modulus distribution further corroborates uniform ionomer coverage, as inhomogeneities would induce larger mass transport resistance. This improvement can be attributed to the decrease of oxygen-containing functional groups on the modified EC300J carbon surface. It is believed to reduce electrostatic repulsion between the carbon particles and the negatively charged sulfonic groups of the ionomer, thereby promoting a more homogeneous dispersion.

The R_{local} at the TPBs and the bulk oxygen transport resistance (r_{bulk}) in porous structures are assessed using limiting current measurement [29, 47] combined with the dual-layer electrodes [28]. The CCLs are fabricated with the Pt/porous carbon, and Pt/Fe graphitized porous carbon catalysts, while DCLs are fabricated with their corresponding carbon supports, with no electrochemical reaction occurring in DCLs. All MEAs of the catalysts for oxygen transport measurements with the cathode loading of 0.05 $mg_{Pt}·cm^{-2}$ and the area of 1 cm × 2 cm are tested under H_2/4 mol% O_2–N_2 mixed gas, 67% RH, 150 kPa_{abs}, and 80 °C. The high flow rate for the cathode and anode is 0.8 and 1.5 $L·min^{-1}$ to carry away vapor and homogenize the oxygen concentration in the flow field.

Based on Fick's Law and Faraday's Law, the total oxygen transport resistance (R_{total}) in the cathode can be figured out accounting for the limiting current density (i_{lim}) when the concentration of oxygen on the Pt surface is zero. In terms of the configuration of the dual-layer electrodes fuel cell, it could be separated into resistance in the CCL (R_{CCL}), DCL (R_{DCL}), GDL (R_{GDL}), and flow channel ($R_{Channel}$) as Eq. (2)

$$R_{total} = 4F\frac{c_{O_2}}{i_{lim}} = R_{CCL} + R_{DCL} + R_{GDL} + R_{Channel} \quad (2)$$

where F is the Faraday constant and c_{O_2} is the molar concentration of oxygen in the flow field.

Due to the fact that DCLs do not undergo electrochemical reactions and that oxygen must pass through the DCL in order to reach the CCL, where the reaction happens, R_{DCL} only carries the bulk oxygen transport resistance, which is proportional to the thickness of the DCL, as shown in Eq. (3). Therefore, the bulk oxygen transport resistance per unit thickness is further expressed as a function of the DCL thickness (h)

$$R_{DCL} = r_{bulk}h \quad (3)$$

In addition, the DCL thicknesses are set to be much higher than

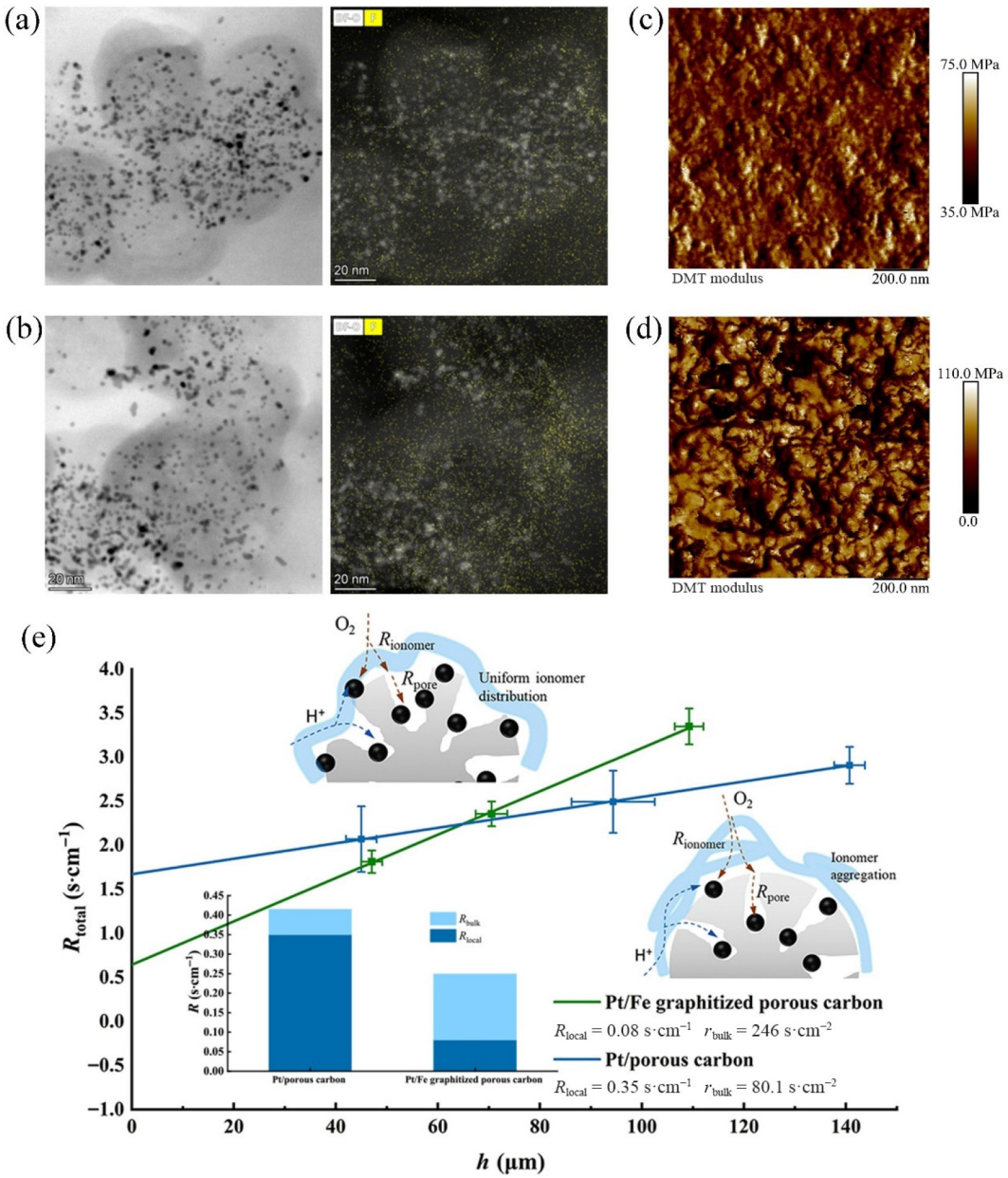

Figure 7 Triple phase boundary characterization for the CCLs based on Pt/porous carbon and Pt/Fe graphitized carbon. STEM image (left) and EDX mapping of F (right) for (a) Pt/porous carbon and (b) Pt/Fe graphitized carbon showing the ionomer and Pt distribution. AFM modulus for CLs based on (c) Pt/porous carbon and (d) Pt/Fe graphitized carbon. (e) Plot of R_{total} vs. h. The anode and cathode reaction gas, flow rate, RH, operating pressure, and temperature are H_2/4 mol% O_2, 0.8/1.5 L·min^{-1}, 67% RH, 150 kPa$_{abs}$, and 80 °C. Insert is the proportion of bulk oxygen transport resistance of the whole CCL ($R_{bulk} = r_{bulk} \cdot h_{CCL}$) and R_{local}, and schematic illustration of R_{local} on TPBs.

that of CCL. Thus, the bulk oxygen transport resistance in CCL is negligible. Equation (3) is further expressed as a function of the DCL thickness

$$R_{total} = R_{local} + r_{bulk} h + R_{GDL} + R_{Channel} \quad (4)$$

Noted that R_{GDL} is determined by the structure and properties of GDLs as well as the compression ratio, which is measured to be 0.31 s·cm^{-1} in our previous work [14], and $R_{Channel}$ is related to the type of flow channel and calculated to be 0.26 s·cm^{-1} based on an empirical formula deduced by Baker et al [29].

Therefore, R_{local} could be calculated according to the intercept in the plot of R_{total} vs. h (Fig. 7(e)) to be 0.35 and 0.08 s·cm^{-2}, for the Pt/porous carbon and Pt/Fe graphitized porous carbon catalysts, respectively. The obvious decrease of R_{local} on the TPBs is related to the optimized interface of ionomer and carbon surface.

For the catalyst outside the pore, R_{local} comes from $R_{ionomer}$, which is usually divided into three steps: (i) oxygen adsorption on gas/ionomer interface, (ii) oxygen diffusion inside the thin ionomer film, and (iii) oxygen adsorption on ionomer/Pt interface. For the catalyst inside the pore, R_{pore} is also prominent in addition to the $R_{ionomer}$. The insert illustration in Fig. 7(e) demonstrates the optimal oxygen transport pathway with the catalysts supported on the graphitized modified carbon. It is the enhanced interaction force between the ionomer and the exterior carbon surface arising from the graphitization that makes the distribution of the ionomer

uniform by adjusting the charge effect and thus reducing the $R_{ionomer}$. Further, due to the optimization of the surface structure of the carbon supports, the accessible pore size between 4–7 nm, which is conducive to oxygen transport, increases, resulting in a decrease in R_{pore} in interior pores.

It is noted that the r_{bulk} is calculated according to the slope in the plot in Fig. 7(e) to be 80.1 and 246 s·cm^{-1}, increasing as the carbon supports graphitize. In terms of the TEM images of the catalysts, the carbon particle size is reduced from 36.7 to 27.8 nm due to the thermal corrosion in the treatment process (Figs. S11 and S12 in the ESM). The pore size distribution and porosity (ε) are evaluated using mercury intrusion porosimetry (MIP), as presented in Fig. S13 in the ESM. ε is examined to be 49.8% and 39.6% for DCL with the pristine EC300J and with the modified EC300J, and the pore size in the DCL with the modified EC300J is smaller relative to that with the pristine EC300J. However, the catalyst loading is only 0.08 mg$_{Pt}$·cm^{-2}, and the thicknesses of the CCLs (h_{CCL}) 7 and 8 μm for Pt/porous carbon and Pt/Fe graphitized carbon, respectively, as shown in Fig. S14 in the ESM. The overall oxygen transport resistance in the insert of Fig. 7(e) is still significantly reduced, albeit the r_{bulk} is increased. Therefore, the MEAs with Pt/Fe graphitized porous carbon catalysts posit a balance between oxygen transport in pore structure in CCLs and at the TPBs.

3.5 MEA stability

The stabilities of the catalysts were investigated based on the AST protocol, where the voltage cycling from 1 V up to 1.5 V with 500 mV·s^{-1} at 100% RH and cell temperature of 80 °C, and the anode is fed with H_2 and the cathode with N_2. The polarization curves of the pristine MEAs and after 3000 AST cycles are depicted in Figs. 8(a) and 8(b), and of the commercial catalyst TEC10E30E is depicted in Fig. S15 in the ESM. After 3000 AST cycles, the peak power density loss for the Pt/porous carbon is decreased by 55.2%, while for Pt/graphitized porous carbon, it is decreased by 8.8%. The results indicate that the modified carbon supports possess superior anti-corrosion performance, presumably owing to the formation of a more stable ordered graphitized surface layer with decreased oxygen-containing functional groups [19] compared to the unmodified carbon supports. ECSA (Fig. 8(c)) and mass activity@0.9 V (Fig. 8(d)) of the catalysts before and after AST are compared mainly affected by the catalyst nanoparticles on the carbon supports and ionomer–carbon interaction. The obvious improvement of the mass activity and ECSA stability of Pt/Fe graphitized porous carbon catalyst arises from the alleviation of the weakened anchoring effect of the catalyst on the carbon supports caused by the carbon corrosion, which could result in the catalyst falling off and agglomerating. Figure 8(e) showed that the R_{total} of the MEA based on the Pt/porous carbon increased 45.3%, while the R_{total} of the MEA based on the Pt/graphitized porous carbon catalysts was almost unchanged. A detailed performance comparison is presented in Fig. 8(f). It is believed that the maintained pore structure contributed to the stability of the oxygen transport path. The decreased surface oxidation and oxygen-containing functional groups of the carbon supports prevent the agglomeration of ionomer in the CCLs, thus maintaining the optimized oxygen transport path in the ionomer.

4 Conclusions

Recognizing that the key challenges for enhancing the performance and durability of ultimate PEMFCs lie in achieving a comprehensive ionomer/catalyst interface, the essential and fundamental challenge with porous carbon supports is to build a stable TPBs featuring uniform ionomer coverage and accessible porous structure on carbon support surface. In this study, we presented a high oxygen transport electrode with long-term stability for high-power and low Pt-loading PEMFCs based on carbon support modification. The surface graphitization is successfully catalyzed by Fe at 900 °C, thereby overcoming the limitations associated with the excessively high temperatures required in traditional graphitization processes. The slight thermal corrosion of

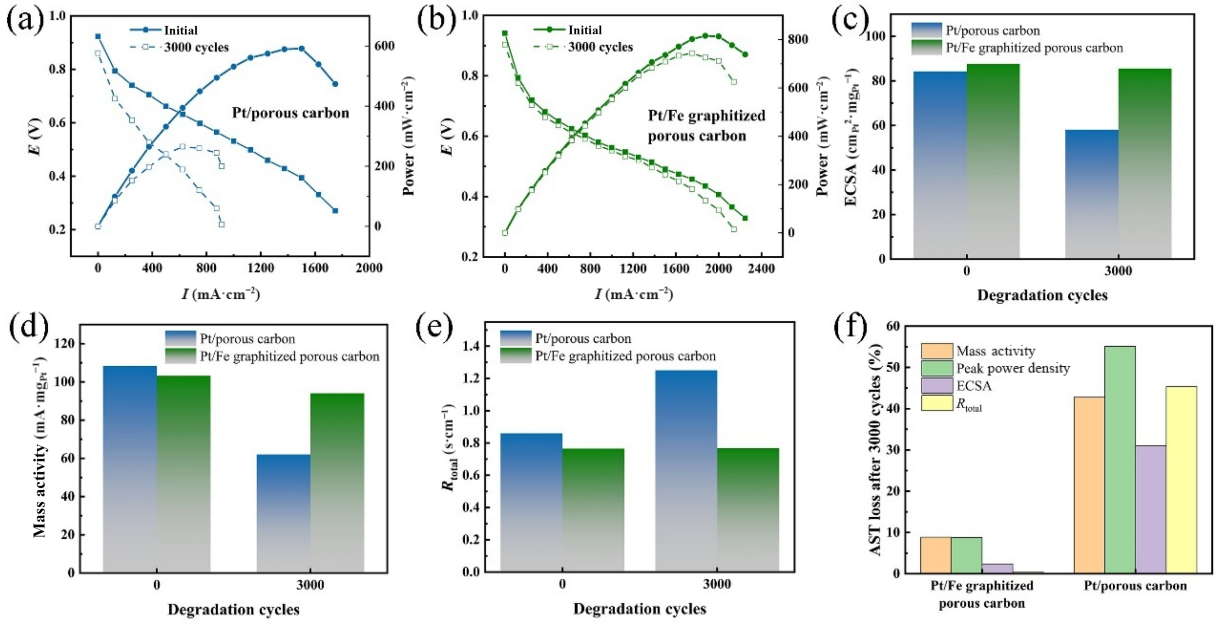

Figure 8 Stability of the fuel cell performance for the Pt/porous carbon, and Pt/Fe graphitized porous carbon catalysts with triangular wave scanning (1.0–1.5 V, 500 mV·s^{-1}) over 3000 degradation cycles. Polarization curves before and after degradation for (a) Pt/porous carbon and (b) Pt/Fe graphitized porous carbon catalysts. Performance comparison of (c) ECSA, (d) mass activity, and (e) R_{total}. (f) Normalized AST loss after 3000 cycles.

carbon supports in this process facilitates the conversion of micropores into accessible pores, leading to an increase in desired pore size between 4 and 7 nm. The results show that R_{local} decreased significantly from 0.35 to 0.08 s·cm^{-1} compared to the catalyst with conventional carbon supports EC300J as baseline catalyst (Pt/porous carbon). It is attributed to the optimized pore size and uniform ionomer distribution on carbon surface after Fe graphitization modification, providing facile and efficient oxygen transport at the TPBs. The polarization curve shows 38% higher performance than the baseline catalyst under standard operating conditions. The higher degree of graphitization also contributes to enhanced durability, resulting in a reduced performance loss (8.8%) after 3000 high-potential degradation cycles compared to the baseline electrode (55.2%).

Electronic Supplementary Material: Supplementary material (further details of TEM morphology, Roman spectra and pore size distribution of EA carbon support, XRD and pore size distribution with different amount of $Fe(NO_3)_3$, SEM images, and polarization curves) is available in the online version of this article at https://doi.org/10.26599/NR.2026.94908445.

Data availability

All data needed to support the conclusions in the paper are presented in the manuscript and the Electronic Supplementary Material. Additional data related to this paper may be requested from the corresponding author upon request.

Acknowledgements

This work is supported by the National Key Research and Development Program of China (No. 2021YFB4001301) and the China Postdoctoral Science Foundation (No. 2024M761941).

Declaration of competing interest

All the contributing authors report no conflict of interests in this work.

Author contribution statement

H. Y. L.: Data curation, project administration, validation, writing manuscript, experimental design, funding acquisition. J. B. Y.: Data curation, manuscript revision. S. Y.: Experimental design. E. P. W.: Data curation. X. J. C.: Experimental design. L. X. L.: Validation. X. H. Y.: Validation. S. Y. S.: Project administration, funding acquisition. J. L. Z.: Experimental design, manuscript revision, project administration. All the authors have approved the final manuscript.

Use of AI statement

None.

References

[1] Jewell, J.; McCollum, D.; Emmerling, J.; Bertram, C.; Gernaat, D. E. H. J.; Krey, V.; Paroussos, L.; Berger, L.; Fragkiadakis, K.; Keppo, I. et al. Limited emission reductions from fuel subsidy removal except in energy-exporting regions. *Nature* **2018**, *554*, 229–233.

[2] Wang, Y.; Pang, Y. H.; Xu, H.; Martinez, A.; Chen, K. S. PEM Fuel cell and electrolysis cell technologies and hydrogen infrastructure development—A review. *Energy Environ. Sci.* **2022**, *15*, 2288–2328.

[3] Suter, T. A. M.; Smith, K.; Hack, J.; Rasha, L.; Rana, Z.; Angel, G. M. A.; Shearing, P. R.; Miller, T. S.; Brett, D. J. L. Engineering catalyst layers for next-generation polymer electrolyte fuel cells: A review of design, materials, and methods. *Adv. Energy Mater.* **2021**, *11*, 2101025.

[4] Jiao, K.; Xuan, J.; Du, Q.; Bao, Z. M.; Xie, B.; Wang, B. W.; Zhao, Y.; Fan, L. H.; Wang, H. Z.; Hou, Z. J. et al. Designing the next generation of proton-exchange membrane fuel cells. *Nature* **2021**, *595*, 361–369.

[5] Zhang, C. L.; Shen, X. C.; Pan, Y. B.; Peng, Z. M. A review of Pt-based electrocatalysts for oxygen reduction reaction. *Front Energy* **2017**, *11*, 268–285.

[6] USDOE. Multi-year research, development, and demonstration plan: 2016 fuel cells section [Online]. Fuel Cell Technologies Office: Washington, DC, 2017. https://www.energy.gov/sites/prod/files/2017/05/f34/fcto_myrdd_fuel_cells.pdf (accessed Dec 16, 2025).

[7] Weber, A. Z.; Kusoglu, A. Unexplained transport resistances for low-loaded fuel-cell catalyst layers. *J. Mater. Chem. A* **2014**, *2*, 17207–17211.

[8] Kulikovsky, A. Impedance and resistivity of low-Pt cathode in a PEM fuel cell. *J. Electrochem. Soc.* **2021**, *168*, 044512.

[9] Kong, F. T.; Cui, X. Z.; Huang, Y. F.; Yao, H. L.; Chen, Y. F.; Tian, H.; Meng, G.; Chen, C.; Chang, Z. W.; Shi, J. L. N-doped carbon electrocatalyst: Marked ORR activity in acidic media without the contribution from metal sites. *Angew. Chem., Int. Ed.* **2022**, *61*, e202116290.

[10] Shui, J. L.; Wang, M.; Du, F.; Dai, L. M. N-doped carbon nanomaterials are durable catalysts for oxygen reduction reaction in acidic fuel cells. *Sci. Adv.* **2015**, *1*, e1400129.

[11] Zhao, Z. P.; Hossain, M. D.; Xu, C. C.; Lu, Z. J.; Liu, Y. S.; Hsieh, S. H.; Lee, I.; Gao, W. P.; Yang, J.; Merinov, B. V. et al. Tailoring a three-phase microenvironment for high-performance oxygen reduction reaction in proton exchange membrane fuel cells. *Matter* **2020**, *3*, 1774–1790.

[12] Yu, X. W.; Ye, S. Y. Recent advances in activity and durability enhancement of Pt/C catalytic cathode in PEMFC: Part I. Physico–chemical and electronic interaction between Pt and carbon support, and activity enhancement of Pt/C catalyst. *J. Power Sources* **2007**, *172*, 133–144.

[13] Wang, Y. J.; Zhao, N. N.; Fang, B. Z.; Li, H.; Bi, X. T.; Wang, H. J. Carbon-supported Pt-based alloy electrocatalysts for the oxygen reduction reaction in polymer electrolyte membrane fuel cells: Particle size, shape, and composition manipulation and their impact to activity. *Chem. Rev.* **2015**, *115*, 3433–3467.

[14] Li, H. Y.; You, J. B.; Cheng, X. J.; Luo, L. X.; Yan, X. H.; Yin, J. W.; Shen, S. Y.; Zhang, J. L. Unraveling the effects of carbon corrosion on oxygen transport resistance in low Pt loading proton exchange membrane fuel cells. *ACS Appl. Mater. Interfaces* **2024**, *16*, 540–554.

[15] Huang, J.; Li, Z.; Zhang, J. B. Review of characterization and modeling of polymer electrolyte fuel cell catalyst layer: The blessing and curse of ionomer. *Front. Energy* **2017**, *11*, 334–364.

[16] Ott, S.; Du, F. M.; Luna, M. L.; Dao, T. A.; Cuenya, B. R.; Orfanidi, A.; Strasser, P. Understanding the performance increase of catalysts supported on N-functionalized carbon in PEMFC catalyst layers. *J. Electrochem. Soc.* **2022**, *169*, 054520.

[17] Ott, S.; Orfanidi, A.; Schmies, H.; Anke, B.; Nong, H. N.; Hübner, J.; Gernert, U.; Gliech, M.; Lerch, M.; Strasser, P. Ionomer distribution control in porous carbon-supported catalyst layers for high-power and low Pt-loaded proton exchange membrane fuel cells. *Nat. Mater.* **2020**, *19*, 77–85.

[18] Li, C. Z.; Yu, K.; Bird, A.; Guo, F.; Ilavsky, J.; Liu, Y. D.; Cullen, D. A.; Kusoglu, A.; Weber, A. Z.; Ferreira, P. J. et al. Unraveling the core of fuel cell performance: Engineering the ionomer/catalyst interface. *Energy Environ. Sci.* **2023**, *16*, 2977–2990.

[19] Bai, J. L.; Ke, S. J.; Song, J.; Wang, K.; Sun, C. Y.; Zhang, J. K.; Dou, M. L. Surface engineering of carbon-supported platinum as a route to electrocatalysts with superior durability and activity for PEMFC cathodes. *ACS Appl. Mater. Interfaces* **2022**, *14*, 5287–5297.
[20] Yarlagadda, V.; Carpenter, M. K.; Moylan, T. E.; Kukreja, R. S.; Koestner, R.; Gu, W. B.; Thompson, L.; Kongkanand, A. Boosting fuel cell performance with accessible carbon mesopores. *ACS Energy Lett* **2018**, *3*, 618–621.
[21] Ramaswamy, N.; Gu, W. B.; Ziegelbauer, J. M.; Kumaraguru, S. Carbon support microstructure impact on high current density transport resistances in PEMFC cathode. *J. Electrochem. Soc.* **2020**, *167*, 064515.
[22] Cheng, X. J.; Wei, G. H.; Wang, C.; Shen, S. Y.; Zhang, J. L. Experimental probing of effects of carbon support on bulk and local oxygen transport resistance in ultra-low Pt PEMFCs. *Int. J. Heat Mass Transf.* **2021**, *164*, 120549.
[23] Mohanta, P. K.; Regnet, F.; Jörissen L. Graphitized carbon: A promising stable cathode catalyst support material for long term PEMFC applications. *Materials* **2018**, *11*, 907.
[24] Fuertes, A. B.; Alvarez, S. Graphitic mesoporous carbons synthesised through mesostructured silica templates. *Carbon* **2004**, *42*, 3049–3055.
[25] Yoon, S. B.; Chai, G. S.; Kang, S. K.; Yu, J. S.; Gierszal, K. P.; Jaroniec, M. Graphitized pitch-based carbons with ordered nanopores synthesized by using colloidal crystals as templates. *J. Am. Chem. Soc.* **2005**, *127*, 4188–4189.
[26] Ōya, A.; Marsh, H. Phenomena of catalytic graphitization. *J. Mater. Sci.* **1982**, *17*, 309–322.
[27] Krivoruchko, O. P.; Maksimova, N. I.; Zaikovskii, V. I.; Salanov, A N. Study of multiwalled graphite nanotubes and filaments formation from carbonized products of polyvinyl alcohol via catalytic graphitization at 600–800 °C in nitrogen atmosphere. *Carbon* **2000**, *38*, 1075–1082.
[28] Wang, C.; Cheng, X. J.; Lu, J. B.; Shen, S. Y.; Yan, X. H.; Yin, J. W.; Wei, G. H.; Zhang, J. L. The experimental measurement of local and bulk oxygen transport resistances in the catalyst layer of proton exchange membrane fuel cells. *J. Phys. Chem. Lett.* **2017**, *8*, 5848–5852.
[29] Baker, D. R.; Caulk, D. A.; Neyerlin, K. C.; Murphy, M. W. Measurement of oxygen transport resistance in PEM fuel cells by limiting current methods. *J. Electrochem. Soc.* **2009**, *156*, B991.
[30] Zhang, X.; Guo, L. J.; Liu, H. T. Recovery mechanisms in proton exchange membrane fuel cells after accelerated stress tests. *J. Power Sources* **2015**, *296*, 327–334.
[31] Thambiliyagodage, C. J.; Ulrich, S.; Araujo, P. T.; Bakker, M. G. Catalytic graphitization in nanocast carbon monoliths by iron, cobalt and nickel nanoparticles. *Carbon* **2018**, *134*, 452–463.
[32] Sevilla, M.; Fuertes, A. B. Catalytic graphitization of templated mesoporous carbons. *Carbon* **2006**, *44*, 468–474.
[33] Ōya, A.; Mochizuki, M.; Ōtani, S.; Tomizuka, I. An electron microscopic study on the turbostratic carbon formed in phenolic resin carbon by catalytic action of finely dispersed nickel. *Carbon* **1979**, *17*, 71–76.
[34] Andersen, S. M.; Borghei, M.; Dhiman, R.; Jiang, H.; Ruiz, V.; Kauppinen, E.; Skou, E. Interaction of multi-walled carbon nanotubes with perfluorinated sulfonic acid ionomers and surface treatment studies. *Carbon* **2014**, *71*, 218–228.
[35] Ma, P. C.; Siddiqui, N. A.; Mäder, E.; Kim, J. K. Correlation between electrokinetic potential, dispersibility, surface chemistry and energy of carbon nanotubes. *Compos. Sci. Technol.* **2011**, *71*, 1644–1651.
[36] Neimark, A. V.; Lin, Y. Z.; Ravikovitch, P. I.; Thommes, M. Quenched solid density functional theory and pore size analysis of micro-mesoporous carbons. *Carbon* **2009**, *47*, 1617–1628.
[37] Weidenthaler, C. Pitfalls in the characterization of nanoporous and nanosized materials. *Nanoscale* **2011**, *3*, 792–810.
[38] Ravikovitch, P. I.; Neimark, A. V. Density functional theory model of adsorption on amorphous and microporous silica materials. *Langmuir* **2006**, *22*, 11171–11179.
[39] Fang, B. Z.; Chaudhari, N. K.; Kim, M. S.; Kim, J. H.; Yu, J. S. Homogeneous deposition of platinum nanoparticles on carbon black for proton exchange membrane fuel cell. *J. Am. Chem. Soc.* **2009**, *131*, 15330–15338.
[40] Fan, J. T.; Chen, M.; Zhao, Z. L.; Zhang, Z.; Ye, S. Y.; Xu, S. Y.; Wang, H. J.; Li, H. Bridging the gap between highly active oxygen reduction reaction catalysts and effective catalyst layers for proton exchange membrane fuel cells. *Nat. Energy* **2021**, *6*, 475–486.
[41] Talukdar, K.; Delgado, S.; Lagarteira, T.; Gazdzicki, P.; Friedrich, K. A. Minimizing mass-transport loss in proton exchange membrane fuel cell by freeze-drying of cathode catalyst layers. *J. Power Sources* **2019**, *427*, 309–317.
[42] Ramaswamy, N.; Kumaraguru, S.; Koestner, R.; Fuller, T.; Gu, W. B.; Kariuki, N.; Myers, D.; Dudenas, P. J.; Kusoglu, A. Editors' choice—Ionomer side chain length and equivalent weight impact on high current density transport resistances in PEMFC cathodes. *J. Electrochem. Soc.* **2021**, *168*, 024518.
[43] Ramaswamy, N.; Kumaraguru, S. Materials and design selection to improve high current density performance in PEMFC. *ECS Trans.* **2018**, *85*, 835–842.
[44] Owejan, J. P.; Owejan, J. E.; Gu, W. B. Impact of platinum loading and catalyst layer structure on PEMFC performance. *J. Electrochem. Soc.* **2013**, *160*, F824–F833.
[45] Takeshita, T.; Yano, K.; Kodama, K. Effect of the pore size of mesoporous carbon supports for cathode catalysts on the cell performance of polymer electrolyte fuel cells. *ACS Catal.* **2025**, *15*, 13549–13557.
[46] Islam, M. N.; Mansoor Basha, A. B.; Kollath, V. O.; Soleymani, A. P.; Jankovic, J.; Karan, K. Designing fuel cell catalyst support for superior catalytic activity and low mass-transport resistance. *Nat. Commun.* **2022**, *13*, 6157.
[47] Baker, D. R.; Wieser, C.; Neyerlin, K. C.; Murphy, M. W. The use of limiting current to determine transport resistance in PEM fuel cells. *ECS Trans.* **2006**, *3*, 989–999.